

Bottom-up approach to room-temperature quantum systemsBochao Wei , Chao Li ,* Ce Pei, and Chandra Raman *School of Physics, Georgia Institute of Technology, 837 State Street, Atlanta, Georgia 30332, USA*

(Received 12 December 2022; revised 10 September 2023; accepted 17 October 2023; published 14 November 2023)

We demonstrate a key ingredient in a bottom-up approach to building complex quantum matter using thermal atomic vapors. We isolate and track very slowly moving individual atoms without the aid of laser cooling. Passive filtering enables us to carefully select atoms whose three-dimensional velocity vector has a magnitude below $\bar{v}/20$, where \bar{v} is the mean velocity of the ensemble. Using a photon correlation technique, we can extract the velocity distributions. We can also follow the trajectory of slowly moving single atoms for more than $1\ \mu\text{s}$ within a $25\text{-}\mu\text{m}$ field of view, with no obvious limit to the tracking ability while simultaneously observing Rabi oscillations of these single emitters. In addition, we measure the third-order correlation function of single thermal atoms. Our results demonstrate the power and scalability of thermal ensembles for utilization in quantum memories, imaging, and other quantum information applications through bottom-up approaches.

DOI: [10.1103/PhysRevA.108.053710](https://doi.org/10.1103/PhysRevA.108.053710)**I. INTRODUCTION**

In recent years there has been a surge of interest in room-temperature atomic vapors for applications in quantum information science. In contrast to laser-cooled samples, they are straightforward to fabricate, highly scalable, and can be operated continuously. One can define two broad thrusts to this research: a top-down and a bottom-up approach. The former, which has been adopted in four-wave-mixing experiments [1–4], seeks to engineer collective quantum behavior within the vapor and ignores the discrete nature of the constituent particles. The latter approach seeks to construct a complex quantum system from individual atomic building blocks, for example, optical tweezer arrays [5,6] and trapped ions [7,8]. For thermal vapors, this approach is relatively undeveloped. At issue is the rapid and random thermal motion of the atoms that makes it difficult to track them without the aid of a meter-long atomic beam apparatus [9–11]. If one could address this issue using more modern methods such as a compact and simple vapor cell [12], the possibilities are clearly enormous: A typical rubidium ensemble at $100\text{ }^\circ\text{C}$ contains $O(10^9)$ completely indistinguishable quantum systems within a 1 mm^3 volume. Even a small fraction of such a large ensemble constitutes a huge and readily available resource for quantum information, if it can be harnessed, while simultaneously requiring much lower experimental overhead compared with analogous cold-atom systems. Figure 1(a) illustrates an array of mesoscopic cells within a thermal vapor. The atomic density has been lowered so that each cell contains at most one atom. In our experiment each cell's linear dimension is $25\ \mu\text{m}$. With negligible double occupancy, one effectively has an ensemble of spatially resolved single emitters. However, at

typical thermal velocities of 300 m/s atoms cannot be interrogated for more than approximately 83 ns within one cell, which is too short for most purposes. Moreover, atoms move in random directions and cannot be tracked once they leave their respective cells. Coherence times of quantum memories in thermal vapors are therefore well below $1\ \mu\text{s}$ due to this motion-induced dephasing [4].

Figure 1(b) shows the approach taken in this experimental work to address motion-induced dephasing. By selecting a subensemble of atoms from an atomic beam whose three-dimensional velocity vector is 20 times smaller in magnitude than the mean, we extended the observation time to more than $1\ \mu\text{s}$. We simultaneously tracked a single atom across more than one cell, which was possible since all the atoms traveled in the same direction. However, since these atoms continue to move undisturbed along the axis for many centimeters before colliding with either background gas or the vacuum wall, the potential exists to increase the interaction time by several orders of magnitude beyond what has been achieved thus far with thermal vapors [4]. As a proof of our method, we measured quantum-mechanical antibunching and the correlated photon emission from a single atom. We also observed large values of the second-order $g^{(2)}(\tau)$ and third-order coherences $g^{(3)}(\tau_1, \tau_2)$. This indicates the potential for this system to be a simple source of photon pairs or triplets when suitably selected and prepared.

This tracking method is the key resource needed to envision a bottom-up approach to quantum information. The key point is that tracking allows us to gain precise classical information about where the atoms are and thus to utilize them downstream. Even tracking two atoms can provide a significant utility. For example, in Fig. 1(c) we show a protocol whereby tracking generates indistinguishable photon-pair states with a relatively simple setup that requires minimal resources. In the first step, we illuminate cells *a* and *b*. Slowly moving atoms in these cells then emit light via resonance fluorescence. Heralded detection of a pair of photons at

*Present address: Research Laboratory of Electronics, Massachusetts Institute of Technology, Cambridge, MA 02139, USA.

†Corresponding author: craman@gatech.edu

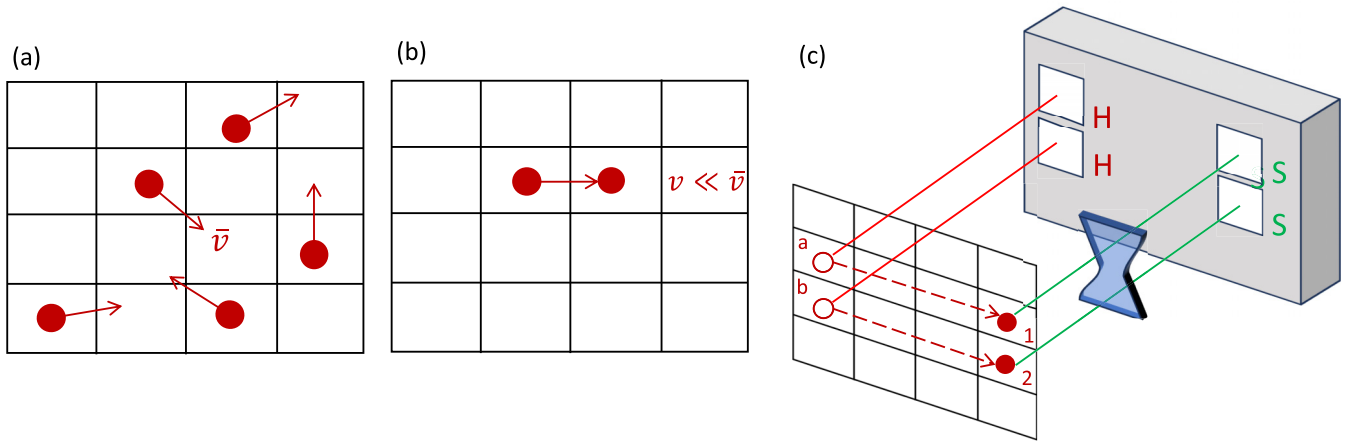


FIG. 1. Concept of the bottom-up approach to room-temperature quantum information processing with neutral atoms. Shown are arrays of mesoscopic cells of volume V containing less than one atom per cell on average. The average cell occupancy $f = n/V$, where n is the atomic density, should be adjusted to be the same for scenarios (a) and (b). (a) Ordinary vapor with mean thermal velocity \bar{v} . (b) Three-dimensional velocity selection of atoms with $v \ll \bar{v}$ that has been accomplished in this work. Atoms are tracked from one cell to the next. (c) Application of tracked slow atoms to photon-pair generation. Upon receiving a pair of heralding photons (H), the occupation probability of two cells a and b by one atom each becomes 1. Tracking is then used to determine the exact time when these atoms will enter cells 1 and 2. Single-photon pairs are then generated and used to generate a quantum image of a target (the hourglass) onto two signal detectors (S). Additional optical elements used for imaging are not shown.

detectors marked H confirms the presence of one atom in each cell. Tracking can then be used to determine the arrival time of the two atoms at two downstream cells 1 and 2. Due to the atoms' low velocity, the timing accuracy requirements can be considerably relaxed, around $1 \mu\text{s}$. A short excitation pulse of light then generates a correlated two-photon state $|1_1, 1_2\rangle$. Here 1_i , for $i = 1, 2$, indicates a single photon transversely localized to cell i and propagating toward the detector.

Using a single-photon camera for detection [13,14], these photon pairs can be used for image reconstruction of a target [the hourglass-shaped object in Fig. 1(c)] similar to single-photon down-conversion sources [15]. The quantum advantage of such single-photon Fock states has been discussed extensively in the literature. Minimizing sample exposure and sub-shot-noise detection are key improvements that can be achieved [16]. Our approach can in principle even be scaled up to larger photon-number states n (e.g., one photon from each atom in n cells), which would be a very intriguing and novel light source. Finite detection efficiency will have to be considered for such applications. In Appendix C we show details of how the tracking procedure can create high-purity photon pairs in the state $|1_1, 1_2\rangle$.

II. SLOW SINGLE ATOMS IN THERMAL ATOMIC BEAMS

The schematic of the experimental setup for demonstrating tracking is shown in Fig. 2(a). We employ a miniature atomic beam device based on the chip-scale cascaded collimator [17], a two-dimensional passive collimation device. This miniature device can be inserted directly into a $12 \times 12 \times 42 \text{ mm}^3$ cuboid shape glass vacuum cell. The collimator consists of 20 channels, each with a cross section of $100 \times 100 \mu\text{m}^2$, resulting in a beam with a narrow divergence angle ($\theta_{1/2} = 0.013 \text{ rad}$, corresponding to a transverse velocity spread of only $\pm 4 \text{ m/s}$).

With an atomic beam, we can select atoms whose longitudinal velocity is substantially lower than the average. The velocity selection combined with the two-dimensional passive filtering with the collimator can isolate atoms with a small three-dimensional velocity vector. To achieve single emitter dynamics, we ensure that the mean number of atoms in the detection region ($N \ll 1$) by reducing the oven temperature.

The ^{87}Rb D_2 line transition diagram and experimental procedure are shown in Fig. 2(b). A Doppler-free pump beam

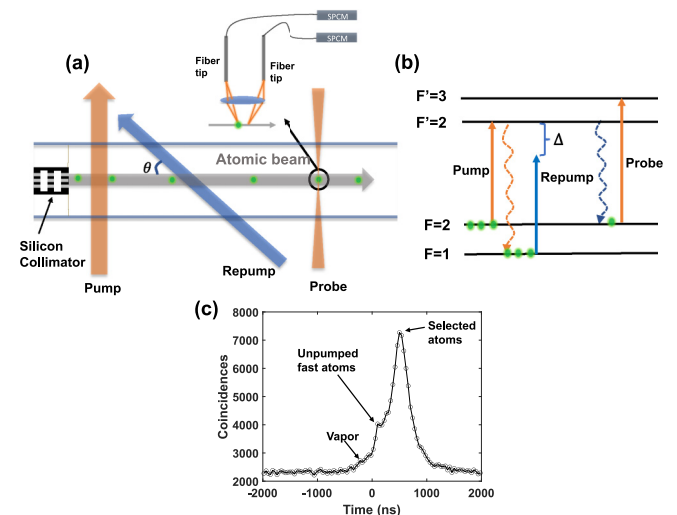


FIG. 2. Selecting and measuring single slow atoms. (a) Schematic of the experiment. The angle between the repump and the atomic beam is $\theta = 47^\circ$. Two cleaved fiber tips are placed on the image plane of the imaging system with a numerical aperture of 0.42. (b) Energy levels involved. The repump is detuned by Δ to select a certain group of atoms. (c) Raw coincidences with different time delays from two SPCMs at $\Delta = -80 \text{ MHz}$.

first pumps all atoms into the hyperfine $F = 1$ state, while an angled repump beam then selectively pumps atoms back to $F = 2$ depending on their longitudinal velocity. Finally, a Doppler-free probe beam perpendicular to the atomic beam couples the $F = 2 \rightarrow F' = 3$ transition to detect the selected atoms. The selected atoms are expected to have a velocity center at $v_c = \frac{-\Delta}{k \cos \theta}$, where $\Delta < 0$ and k are the linear detuning and the wave number of the repump beam, respectively, and θ is the angle between the repump and the atomic beam. Low velocities were selected by decreasing the detuning $|\Delta|$ toward 0.

The ratio of atoms with a velocity below 30 m/s in a thermal rubidium atomic beam is very small (approximately equal to 10^{-5}). It is hard to observe these atoms with normal Doppler-sensitive spectroscopy, as it will be limited by electronic noise, vapor contributions, and the fluorescence from ^{85}Rb . Here we demonstrate a single-atom photon correlation method to track their motion across two cells defined in Fig. 1(b). In our work we utilize optical fibers for light collection over a small distance, an approach that can more easily be scaled up to multiple zones.

Two bare fibers are cleaved and fixed on a plastic holder to keep their distance at 450 μm . This holder is then fixed on the image plane of the microscope and forms two detection regions separated by $d \approx 55 \mu\text{m}$ in the plane of the atoms, as shown in Fig. 2(a). The other end of each fiber is connected to a single-photon counting module (SPCM) where the detected photons are time tagged and analyzed.

When a single atom passes through two detection regions, the photons collected from the two fibers will contribute to time-ordered coincidences with a delay $\tau = \frac{d}{v}$. The accidental coincidences from laser scattering, detector dark counts, etc., do not depend on time delay and can be subtracted later. The focused probe beam has a beam diameter of $2w \approx 120 \mu\text{m}$ that overlaps both detection regions. Figure 2(c) shows the raw coincidence data for $\Delta = -80 \text{ MHz}$. The peak around +500 ns is the contribution from velocity-selected atoms with a center velocity $v = \frac{d}{\tau} \approx 100 \text{ m/s}$. Some fast atoms in the atomic beam escape the pumping process and contribute to the small bump at around +100 ns. During the data acquisition time, a small rubidium vapor gradually builds up and contributes to coincidences with both positive and negative time delays around zero. This vapor could be removed in future experiments by adding some graphite to the vacuum cell.

We can analyze the second-order temporal coherence between SPCM A and SPCM B:

$$g_{AB}^{(2)}(\tau) = \frac{\langle I_A(t)I_B(t + \tau) \rangle}{\langle I_A(t) \rangle \langle I_B(t + \tau) \rangle}. \quad (1)$$

Here $g_{AB}^{(2)}(\tau)$ measures the distribution of coincidences with time delay τ and $g_{AB}^{(2)}(\infty) \rightarrow 1$ represents accidental coincidences. The correlated part $g_{AB}^{(2)}(\tau) - g_{AB}^{(2)}(\infty)$, after normalization, is the coincidence probability density in the time domain $n_{AB}(\tau)$. Given $n_{AB}(\tau)d\tau = n_{AB}(v)dv$ and $\tau = \frac{d}{v}$, we can derive $n_{AB}(v)$, which is the number density of coincidences contributed by atoms whose velocity is v .

The coincidences generated by each atom are proportional to the square of transit time through a single fiber's detec-

tion region, whose diameter is d_f . Then the atom probability density $\rho(v)$ for the flux is derived from coincidence data by using $n_{AB}(v) \propto \rho(v) \frac{d_f^2}{v^2}$ (check Appendix B for details).

For $\Delta = -80 \text{ MHz}$ and an oven temperature of 100°C , the data for $n_{AB}(v)$ are shown in Fig. 3(a). It shows the photon coincidences contributed by atoms with velocities from 0 to 250 m/s. Figure 3(d) shows the calculated atom probability density distribution $\rho(v)$. Compared with the original thermal atomic beam velocity distribution [Fig. 3(d) inset], the selected atoms have a much lower velocity: The peak is at 106 m/s, which agrees reasonably well with the theoretical expectation of 92 m/s.

To select even slower atoms, we use $\Delta = -20$ and -10 MHz , whose data for $n_{AB}(v)$ are shown in Figs. 3(b) and 3(c). The coincidences have shifted to lower velocities, with the peak occurring at 30 and 20 m/s, respectively. The corresponding $\rho(v)$ are shown in Figs. 3(e) and 3(f). Compared with the coincidence $n_{AB}(v)$, the atom probability density distribution is broader and has bigger tails at high velocities. The reason is that slower atoms contribute more coincidences. Thus, the peak locations for $n_{AB}(v)$ are closer to 0 and the peaks are narrower. The expected peak of the atom probability density is at 23 and 12 m/s for Figs. 3(e) and 3(f), while the actual peak locations are both around 50 m/s.

Several nonidealities limited the velocity selection purity. The imperfection in imaging can cause a small probability of detecting photons from atoms between two fiber tips, creating spurious coincidences similar to ultrafast atoms. Some fast atoms managed to avoid being optically pumped through the pump beam, and the background rubidium vapor within the small glass chamber increased with time during the experiment. After averaging for several hours, the correlation method could distinguish the small correlated signals, but some faster atoms inevitably shifted the peak location and caused the long tail in Figs. 3(e) and 3(f). Nonetheless, atoms with velocities around 15 m/s can clearly be observed, as shown in the insets of Figs. 3(e) and 3(f). This demonstrates that we can isolate and directly observe slow atoms with a velocity less than $\bar{v}/20$, where \bar{v} is the mean velocity of the unselected atomic beam.

III. PHOTON STATISTICS

We now demonstrate the unique photon statistics of single atoms in the atomic beam. A key signature of single atoms is the photon antibunching effect [18]. In order to measure the second-order correlation function $g^{(2)}(\tau)$, the collector with two fiber tips is replaced by a single fiber tip that is connected to a 50:50 fiber splitter and two SPCMs to achieve a Hanbury Brown–Twiss configuration. The field of view has a diameter $d_f \approx 25 \mu\text{m}$.

The $g^{(2)}(\tau)$ of an unfiltered thermal atomic beam was first measured by removing the pump and repump beams and reducing the oven temperature to 78°C to achieve $\langle N \rangle < 1$. The data are shown in Fig. 4(a). For classical light the condition $g_2(\tau) \leq g_2(0)$ must be met [19]. Therefore, the observed dip around $\tau = 0$ is the quantum-mechanical antibunching effect from single atoms [18,20]. After an emission event, an atom needs time to be reexcited to emit a second photon,

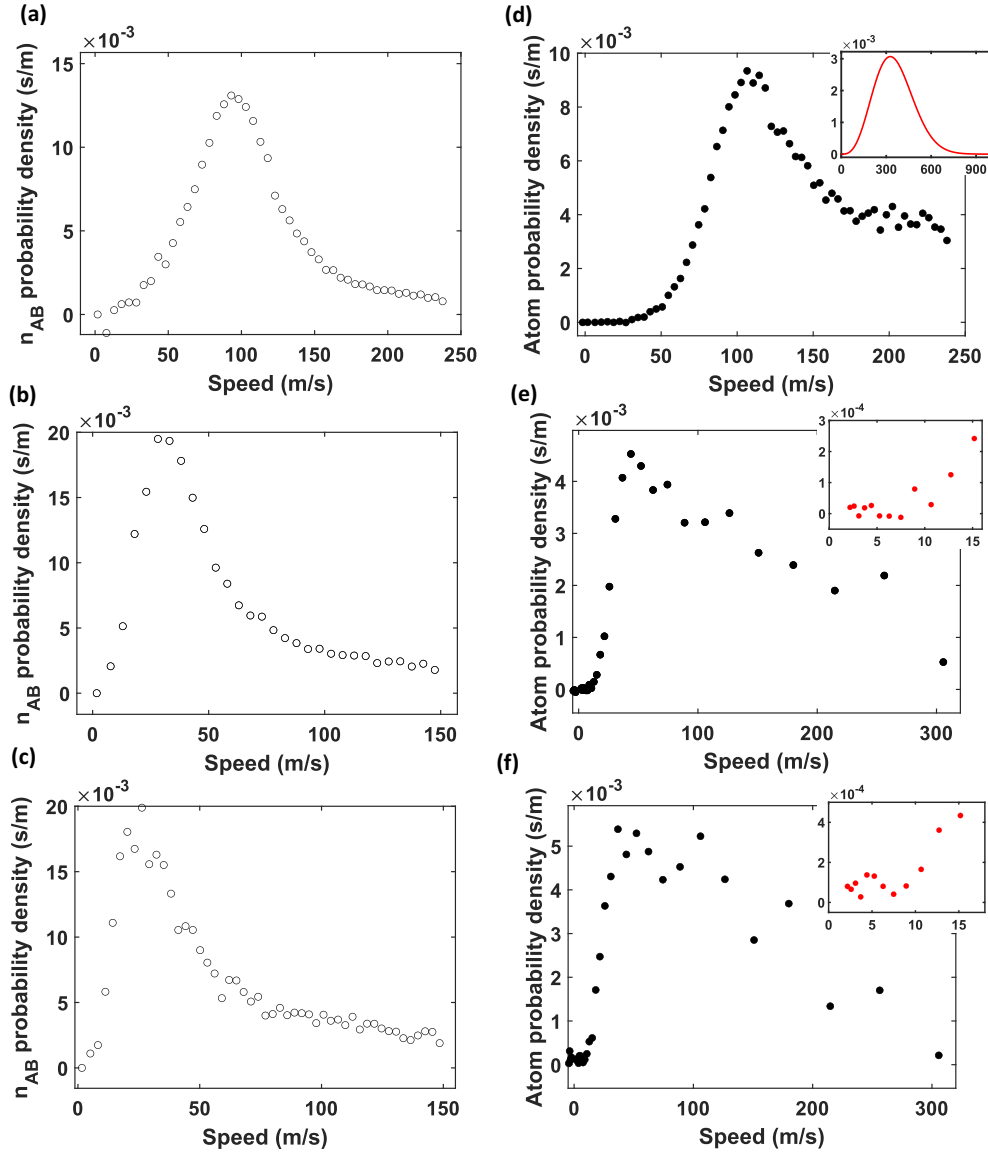


FIG. 3. Atomic velocities measured by correlations. Coincidence distributions in the velocity domain are shown for detunings (a) $\Delta = -80$ MHz, (b) $\Delta = -20$ MHz, and (c) $\Delta = -10$ MHz. The peak velocity shifts from 93 m/s to 30 m/s to 20 m/s. (d)–(f) Corresponding atom probability density distributions. In (d) the peak velocity is 106 m/s, while the inset shows the original thermal distribution at 100 °C. The insets in (e) and (f) are zoomed-in plots of the low-velocity region.

and therefore the maximum of $g^{(2)}(\tau)$ occurs around the first half Rabi cycle. At zero time delay, $g^{(2)}(0) = 1$ rather than 0 because the atomic beam follows the Poisson distribution, and the single emitter condition is not always satisfied [20].

In comparison with trapped-atom systems [21–23], the peak value of $g^{(2)}(\tau)$ observed at $\tau = \tau_{\max} \approx 12$ ns is much larger, as high as 10 for the unfiltered thermal atom data. Such a large value is comparable to correlated photon pairs using four-wave mixing in vapor cells [1,24] and much larger than collective effects in thermal vapor [25]. This is because the accidental coincidences scale with $\langle N \rangle^2$, while the correlated coincidences scale with $\langle N \rangle$. Thus, in an atomic beam where $\langle N \rangle \ll 1$, the ratio of correlated coincidences is much higher. With the Poisson process averaging and transit time correction, the $g^{(2)}(\tau)$ for a thermal atomic beam can be written as

(see Appendix A for derivation)

$$g^{(2)}(\tau) = \xi(\tau) \frac{g_{\text{single}}^2(\tau)}{\langle N \rangle} + 1, \quad (2)$$

where $\xi(\tau)$ is the transit time correction factor whose full expression is given in Appendix A, $g_{\text{single}}^{(2)}(\tau)$ is the second-order coherence function of a single stationary atom, and $\langle N \rangle$ is the mean number of atoms in the field of view. We can learn two things from Eq. (2). One is that $g^{(2)}(\tau) - 1$ is inversely proportional to the average atom number $\langle N \rangle$ and the high $g^{(2)}(\tau)$ value only appears when $\langle N \rangle < 1$. Second, the small ratio $g^{(2)}(0)/g^{(2)}(\tau_{\max}) \approx 0.1$ indicates a high purity of single-atom emission and low contamination by multiatom events. For an ideal single emitter, this ratio is zero.

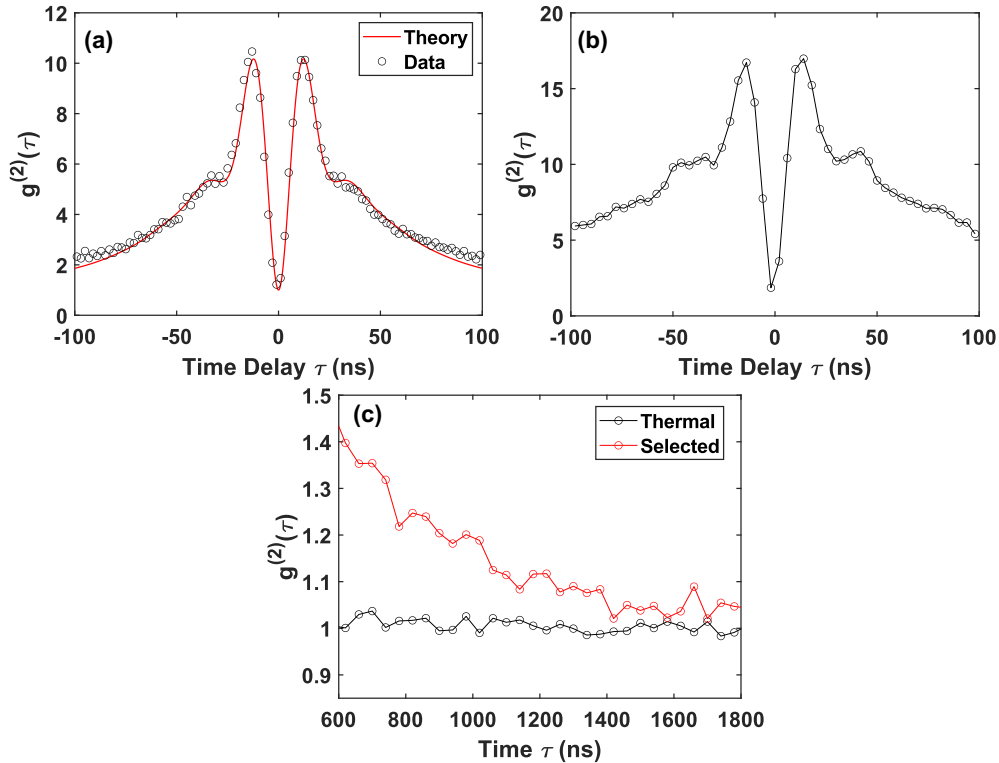


FIG. 4. (a) Plot of $g^{(2)}(\tau)$ with the thermal atomic beam at 78 °C. The time bin size is 2 ns. The red line is the theory curve with $\langle N \rangle = 0.138$ and $L = 25 \mu\text{m}$. (b) Plot of $g^{(2)}(\tau)$ with selected atoms at 100 °C. The selected atoms are more confined in space and suffer less intensity variance in the probe beam. Thus, the second Rabi peak is more visible. The time bin size is 4 ns. (c) Plot of $g^{(2)}(\tau)$ for thermal and selected atoms together with long time delays.

To confirm and compare this effect, the velocity selection scheme was used to measure the $g^{(2)}(\tau)$ for slow atoms at a repump detuning $\Delta = -20$ MHz [see Fig. 4(b)]. The $g^{(2)}(\tau)$ peak is even higher, reaching 17, due to a smaller averaged atom number, with $g^{(2)}(0)/g^{(2)}(\tau_{\text{max}}) \approx 0.06$. Since the transit time for slow atoms is much longer, $g^{(2)}(\tau)$ also decays more slowly at long τ . Figure 4(c) shows the comparison between the $g^{(2)}(\tau)$ of thermal atoms and selected atoms. The correlated photons can be seen for $\tau > 1000$ ns, coming from atoms with $v < 25$ m/s. This shows that we can observe correlated photons from a single atom for longer than 1 μs .

The time delay between the photon pairs can be tuned by the probe laser intensity. With the thermal beam at 78 °C and a probe laser power of 7 μW , the collected photon pairs have a rate of 0.16 pairs per second per fiber. The rate can be improved quadratically with the collecting efficiency and the simplicity and small size of the source should not be overlooked. One can also readily multiplex the output of several cells, for example, by adding more fibers. Moreover, unlike spontaneous parametric down-conversion sources [15,26], this system has a very narrow linewidth and is ideally suited for interaction with rubidium atoms.

Multiphoton generation has been a longstanding challenge in the quantum optics field [27–29]. Cold atoms in optical cavities have been shown to generate multiphoton streams [30]. We expect our system to sequentially generate correlated photons that are indistinguishable from one another and that could be useful for quantum applications such as multiphoton interference [31]. Here we demonstrate the generation of three

photons in short succession to one another. The third-order correlation function $g^{(3)}(\tau_1, \tau_2)$ measures the temporal correlation of three photons:

$$g^{(3)}(\tau_1, \tau_2) = \frac{\langle I_A(t)I_B(t + \tau_1)I_C(t + \tau_2) \rangle}{\langle I_A(t) \rangle \langle I_B(t + \tau_1) \rangle \langle I_C(t + \tau_2) \rangle}. \quad (3)$$

A high $g^{(3)}(\tau_1, \tau_2)$ value means a high probability of detecting three photons with time delays τ_1 and τ_2 compared with other time delays. The $g^{(3)}$ was measured using two detectors in the Hanbury Brown–Twiss configuration. We recorded the arrival time of photons from SPCM A and SPCM B with an accuracy of 350 ps and a dead time $\Theta \approx 45$ ns. Then, since photons do not distinguish SPCM A and SPCM C, the time tags from SPCM A were used as the time tags for SPCM C. We removed the spurious coincidences at $\tau_2 \approx 0$ and a partial function $g^{(3)}(\tau_1, \tau_2 > \Theta)$ was measured. Due to detector dead time, our measurements were sensitive only to the bunching of the triplets $g_{\text{max}}^{(3)} > 1$ occurring at finite delays and not to the antibunching effect near zero.

Figures 5(a) and 5(b) show the data for the thermal atomic beam and $\Delta = -20$ MHz selected atoms, respectively. The time bin size is $100 \times 100 \text{ ns}^2$ to reduce the shot noise and $g^{(3)}(\tau_1, \tau_2 < \Theta)$ is left blank. The peak around zero results from the three consecutive photons emitted during the transit of single atoms. When $\tau_1 \approx \tau_2$, channel B and channel C will have more coincidences as shown in the $g^2(\tau)$ measurements, resulting in a higher value of three-photon coincidences and a diagonal line in Fig. 5(a). When τ_1 or τ_2 is close to zero, the same reason leads to the brighter lines close to the axis. For

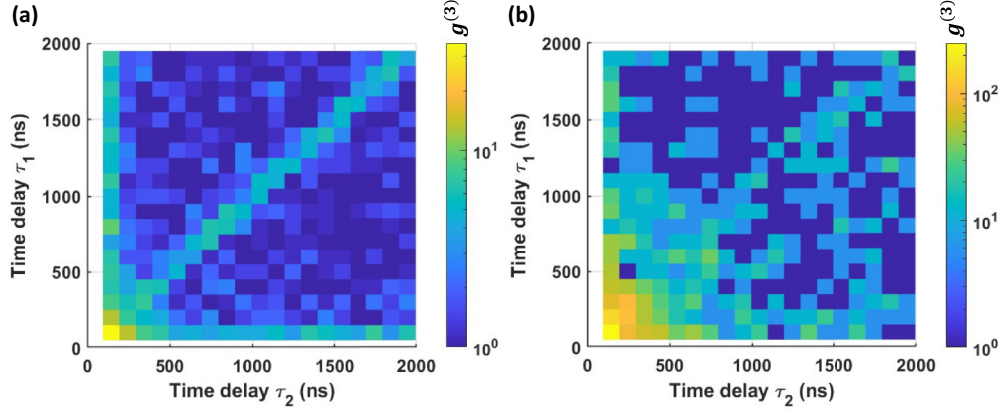


FIG. 5. Measured $g^{(3)}(\tau_1, \tau_2 > \Theta)$. (a) Thermal atomic beam at 78 °C. The maximum $g^{(3)}$ is around 39. (b) Atoms selected using a detuning of $\Delta = -20$ MHz. The maximum $g^{(3)}$ is around 280.

Fig. 5(b), the number of three-photon coincidences is not large enough, and this pattern is blurred by shot noise. Comparing Fig. 5(b) to Fig. 5(a), stronger third-order correlations from slow atoms are detected for large time delays, showing the capability of collecting photon triplets from a single atom for more than 1 μ s.

The maximum values of $g^{(3)}(\tau_1, \tau_2 > \Theta)$ reach 39 and 280 for each case, showing great potential as a photon-triplet source. For the thermal beam, we collected approximately 0.166 triplets per minute. The rate of photon triplets is proportional to the collecting efficiency cubed. Improving the collecting efficiency and adding more fibers in the imaging plane can create bright, narrow-linewidth photon triplets that are compatible with rubidium-based systems.

IV. SUMMARY

We have isolated and detected single slow atoms within a thermal atomic beam and measured their unique photon statistics, showing the possibilities inherent in a bottom-up approach to thermal quantum systems. Improved velocity selectivity can be achieved in the future by adding graphite and using a two-photon Raman transition for pumping.

ACKNOWLEDGMENT

We acknowledge funding from the Air Force Office of Scientific Research through Grant No. FA9550-19-1-0228.

APPENDIX A: EXPERIMENTAL SETUP AND SECOND-ORDER CORRELATION THEORY

As shown in Fig. 6(c), the science chamber is a $12 \times 12 \times 42$ mm³ cuboid glass cell. Both sides of it are bonded to stainless steel bellows to reduce stress. The right port is connected to a Pfeiffer HICUBE 80 ECO pumping station to maintain a pressure of 10^{-7} Torr. The left port is connected to a three-way cross, in which one way is used to insert the atomic oven. The other way is also connected to the same pumping station and assists with pumping the off-axis vapor away. The copper oven delivers rubidium vapor into our silicon cascaded collimator [Fig. 6(a)]. The principle of this

collimator is described in Ref. [17]. The off-axis vapor leaves through the gaps in the collimator while the on-axis atomic beam travels toward the right port. A small box surrounds the collimator to keep the off-axis vapor away from the interaction region.

Two multimode fibers (with a numerical aperture of 0.22 and spaced 105 μ m apart) are stripped and cleaved to have a clean flat end. They are then attached to a fiber holder, which sets their distance to around 450 μ m [Fig. 6(b)]. The two-fiber holder is placed at the image plane of our imaging system and aligned to the direction of our atomic beam. The output of each fiber is fed into a single-photon detection module (SPCM-AQRH-15). The generated transistor-transistor logic pulses are sent into a time interval analyzer (Guidetech GT668) to be time tagged and stored in the hard disk. The time tags are later used to calculate coincidences.

The second-order correlation function $g^{(2)}(\tau)$ is defined as

$$g^{(2)}(\tau) = \frac{\langle I_A(t)I_B(t+\tau) \rangle}{\langle I_A(t) \rangle \langle I_B(t+\tau) \rangle} = \frac{\langle [n_A(t)/\Delta t][n_B(t+\tau)/\Delta t] \rangle}{\langle n_A(t)/\Delta t \rangle \langle n_B(t+\tau)/\Delta t \rangle}, \quad (\text{A1})$$

where $n_{A,B}(t)$ is the number of detected photons from detector A or B in time bin Δt at time t and the intensity $I(t) \propto \frac{n(t)}{\Delta t}$. The effect of $g^{(1)}(\tau)$ can be negligible in our system. For our thermal atomic beam experiment, the background counts are negligible (less than 1%). Thus, we ignore the background counts and only consider photons from the atoms.

For an effusive thermal atomic beam with a given output flux, we define a normalized velocity distribution of the flux $\rho(v)$,

$$\rho(v) = 2 \frac{v^3}{v_0^4} e^{-v^2/v_0^2}, \quad (\text{A2})$$

where $v_0 = \sqrt{\frac{2k_B T}{m}}$, k_B is the Boltzmann constant, m is the mass of the atom, and $\int_v \rho(v) dv = 1$. This distribution is related to the mean number of atoms that transit our collection region per second F_N [see Fig. 6(d)] through the formula $n(v)vA = F_N \rho(v)$, where $n(v)$ is the density of atoms with velocity between v and $v + dv$ and A is the cross-sectional area of the collection region. The relationship between F_N and the average atom number in the field of view $\langle N \rangle$ is then

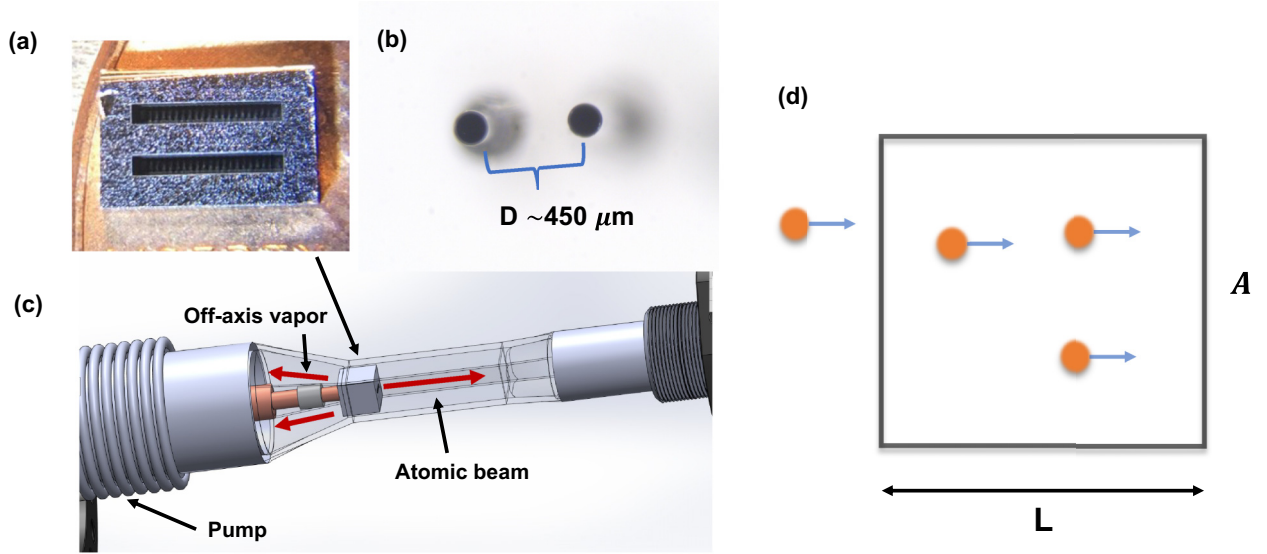


FIG. 6. (a) Image of the cascaded collimator (see Ref. [17] for more details). (b) Microscope image of two fiber tips in the two-fiber detector. (c) Three-dimensional model of the vacuum chamber. (d) Diagram of the collection region of a single fiber showing individual atom transits.

straightforward to calculate,

$$\langle N \rangle = \int_v A L n(v) dv = F_N \int_v \rho(v) \frac{L}{v} dv, \quad (\text{A3})$$

where L is the field of view length in the atomic beam direction.

We calculate the right-hand side of Eq. (A1) by separately evaluating the numerator and denominator, starting with the latter. Here we need the average number of photons detected, which is the product of the mean atom number $\langle N \rangle$, scattering rate R_s , and collection efficiency C_{eff} :

$$\langle n_A(t) / \Delta t \rangle = C_{\text{eff}} R_s F_N \int_v \rho(v) \frac{L}{v} dv. \quad (\text{A4})$$

Moreover, since this average is time independent, the denominator becomes

$$\langle n_A(t) / \Delta t \rangle \langle n_B(t) / \Delta t \rangle = \left(C_{\text{eff}} R_s F_N \int_v \rho(v) \frac{L}{v} dv \right)^2. \quad (\text{A5})$$

To calculate the numerator correctly, we must consider the fluctuating number of atoms in the volume. If $p(N_f)$ is the probability to have N_f atoms in the field of view, then $\langle N \rangle = \sum_{N_f} p(N_f) N_f$. Thus, we can write the numerator as

$$\sum_{N_f} p(N_f) \langle [n_{1A}(t) + n_{2A}(t) + \dots + n_{N_f A}(t)] / \Delta t \{ [n_{1B}(t + \tau) + n_{2B}(t + \tau) + \dots + n_{N_f B}(t + \tau)] / \Delta t \} \rangle, \quad (\text{A6})$$

where $n_{iA}(t)$ represents the number of photons emitted by the i th atom in time bin Δt at time t that reach detector A and similarly for B . Here $n_{iA}(t) n_{jB}(t + \tau)$ are uncorrelated unless $i = j$. Therefore, we can write (A6) as the sum of a correlated

term and an uncorrelated term:

$$\sum_{N_f} p(N_f) \sum_{i=1}^{i=N_f} \langle [n_{iA}(t) / \Delta t] [n_{iB}(t + \tau) / \Delta t] \rangle + \sum_{N_f} p(N_f) \sum_{i \neq j} \langle [n_{iA}(t) / \Delta t] [n_{jB}(t + \tau) / \Delta t] \rangle. \quad (\text{A7})$$

Since all atoms are equivalent, we may write $\langle n_i(t) \rangle = \langle n_j(t + \tau) \rangle$. Therefore, we may calculate everything in terms of just atom 1's emission:

$$\sum_{N_f} p(N_f) N_f \langle [n_{1A}(t) / \Delta t] [n_{1B}(t + \tau) / \Delta t] \rangle + \sum_{N_f} p(N_f) N_f (N_f - 1) \langle n_{1A}(t) / \Delta t \rangle \langle n_{1B}(t + \tau) / \Delta t \rangle. \quad (\text{A8})$$

The relationship between $\langle n_{1A}(t) / \Delta t \rangle$ and $\langle n_A(t) / \Delta t \rangle$ can be derived:

$$\begin{aligned} \langle n_A(t) / \Delta t \rangle &= \sum_{N_f} p(N_f) \langle [n_{1A}(t) + n_{2A}(t) + \dots + n_{N_f A}(t)] / \Delta t \rangle \\ &= \sum_{N_f} p(N_f) N_f \langle n_{1A}(t) / \Delta t \rangle \\ &= \langle N \rangle \langle n_{1A}(t) \rangle. \end{aligned} \quad (\text{A9})$$

Using (A5) and (A9) with (A8), the numerator can be written as

$$\begin{aligned} &\sum_{N_f} p(N_f) N_f \langle [n_{1A}(t) / \Delta t] [n_{1B}(t + \tau) / \Delta t] \rangle \\ &+ \sum_{N_f} p(N_f) \frac{N_f (N_f - 1)}{\langle N \rangle^2} \left(C_{\text{eff}} R_s F_N \int_v \rho(v) \frac{L}{v} dv \right)^2. \end{aligned} \quad (\text{A10})$$

Next we are going to solve the first, correlated term, which is generated by the same atom and is related to its second-order correlation function. We will also calculate the required transit time correction for atoms moving through the field of view. From (A1) we know that for a stationary single atom $g_{\text{single}}^{(2)}(\tau) = \frac{\langle [n'_A(t)/\Delta t][n'_B(t+\tau)/\Delta t] \rangle}{\langle n'_A(t) \rangle \langle n'_B(t+\tau) \rangle}$. Here $\langle n'_A \rangle = \langle n'_{BA} \rangle = C_{\text{eff}} R_s \Delta t$ is the mean number of photons received from a stationary atom without transit time correction. If we then introduce the conditional probability $P(B(\tau)|A)\Delta t$ of detecting the second B photon within a time interval Δt at time delay τ given that the first A photon was detected, we obtain

$$g_{\text{single}}^{(2)}(\tau) = \frac{\langle [n'_A(t)/\Delta t][n'_B(t+\tau)/\Delta t] \rangle}{C_{\text{eff}} R_s C_{\text{eff}} R_s} = \frac{\langle n'_A(t)/\Delta t \rangle P(B(\tau)|A)}{C_{\text{eff}} R_s C_{\text{eff}} R_s} = \frac{P(B(\tau)|A)}{C_{\text{eff}} R_s}. \quad (\text{A11})$$

For one atom transiting the field of view L with velocity v , if a coincidence with a time delay τ is to be detected, the first photon must have been emitted within a distance $L - v\tau$ to allow the second photon at τ to be detected. Thus the transit length for the first photon $\langle n_1(t)/\Delta t \rangle$ is effectively reduced to $L - v\tau$, resulting in a correction factor of $\frac{L-v\tau}{L}$ provided that $\tau < L/v$. No coincidences can be found from the same atom when $v > L/\tau$. Combining $g_{\text{single}}^{(2)}(\tau)$, the transit time correction factor, and Eq. (A4), we finally obtain

$$\begin{aligned} & \langle [n_{1A}(t)/\Delta t][n_{1B}(t+\tau)/\Delta t] \rangle \\ &= \int_{v=0}^{v=L/\tau} dv C_{\text{eff}} R_s \frac{F_N}{\langle N \rangle} \rho(v) \frac{L-v\tau}{L} C_{\text{eff}} R_s g_{\text{single}}^{(2)}(\tau). \end{aligned} \quad (\text{A12})$$

In this equation we may substitute the textbook formula for $g_{\text{single}}^{(2)}(\tau) = 1 - e^{-(3\Gamma/4)\tau} [\cos(\Omega_\Gamma \tau) + \frac{3\Gamma}{4\Omega_\Gamma} \sin(\Omega_\Gamma \tau)]$ [32], where $\Omega_\Gamma = \sqrt{\Omega^2 - (\frac{\Gamma}{4})^2}$, with Ω and Γ the Rabi frequency and spontaneous decay rate, respectively.

Now we put Eq. (A12) back into (A10). We also assume a Poisson distribution of atom numbers in the field of view, for which

$$\sum_{N_f} p(N_f) N_f = \langle N \rangle \quad (\text{A13})$$

and

$$\sum_{N_f} p(N_f) N_f^2 = \langle N \rangle^2 + \langle N \rangle. \quad (\text{A14})$$

With these formulas, Eq. (A10) becomes

$$\begin{aligned} & C_{\text{eff}}^2 R_s^2 F_N \int_{v=0}^{v=L/\tau} \rho(v) \frac{L-v\tau}{v} dv g_{\text{single}}^{(2)}(\tau) \\ &+ \left(C_{\text{eff}} R_s F_N \int_v \rho(v) \frac{L}{v} dv \right)^2. \end{aligned} \quad (\text{A15})$$

Combining the denominator (A5) and the numerator (A15), we get $g^{(2)}(\tau)$:

$$g^{(2)}(\tau) = \left(\frac{\int_{v=0}^{v=L/\tau} (1 - \frac{v\tau}{L}) \frac{\rho(v)}{v} dv}{\int_v F_N \rho(v) \frac{L}{v} dv \int_v \frac{\rho(v)}{v} dv} \right) g_{\text{single}}^{(2)}(\tau) + 1. \quad (\text{A16})$$

From (A3) we can see that the first term in the denominator is actually $\langle N \rangle$. This yields the final expression for $g^{(2)}(\tau)$:

$$g^{(2)}(\tau) = \left(\frac{\int_{v=0}^{v=L/\tau} (1 - \frac{v\tau}{L}) \frac{\rho(v)}{v} dv}{\int_v \frac{\rho(v)}{v} dv} \right) \frac{g_{\text{single}}^{(2)}(\tau)}{\langle N \rangle} + 1. \quad (\text{A17})$$

The transit time correction $\xi(\tau)$ defined in the main text is the term in large parentheses. It includes an extra factor of $1/v$ in the integrand compared with the transit time correction derived in Ref. [20]. Conceptually, it is because slower atoms contribute more photons per transit and thus have a higher weight in the $g^{(2)}(\tau)$. Monte Carlo wave-function simulation is also implemented, and our transit time correction factor fits well with the simulation result (see Fig. 9 in Appendix B).

We then fit this formula to our 78 °C thermal atomic beam data. The averaged atom number $\langle N \rangle$, the field of view L , and the Rabi frequency Ω in $g_{\text{single}}^{(2)}(\tau)$ are fitted to the data, while $\rho(v)$ is the 78 °C atomic beam Maxwell-Boltzmann velocity distribution. Because of the intensity variance in the collecting region, the $g_{\text{single}}^{(2)}(\tau)$ is averaged over a Gaussian-distributed Rabi frequency Ω . The fitted parameters are $\langle N \rangle = 0.138$ and $L = 25 \mu\text{m}$ and Ω is a Gaussian distribution with $\mu = 6\Gamma$ and $\sigma = 1.5\Gamma$ (here Γ is the spontaneous decay rate and μ and σ are the mean and standard deviations of the Gaussian distribution). The theory curve together with the experimental data is shown in Fig. 4(a) in the main text.

APPENDIX B: TWO-FIBER DETECTOR DATA PROCESSING AND MONTE CARLO WAVE-FUNCTION SIMULATION

Similar to the single-fiber second-order correlation theory, here we start with a formula for the coincidence distribution $C(\tau)d\tau$ in the time domain and convert the coincidences into the velocity domain later. As before, we ignore the background counts and only consider photons from the atomic beam. We set the field of view of the fiber to be d_f and the distance between two fibers in the objective plane to be d . We make the approximation that $d_f/d \ll 1$. Two components contribute to the coincidences:

$$C(\tau)d\tau = (\text{uncorrelated term}) + (\text{correlated term}). \quad (\text{B1})$$

The first uncorrelated term is the accidental coincidences generated by randomly having atoms at fiber A and atoms at fiber B at the same time. This term has no relationship to time delay τ and can be written as

$$\begin{aligned} (\text{uncorrelated term}) &= \int_v C_{\text{eff}} R_s F_N \rho(v) \frac{d_f}{v} dv \\ &\int_v C_{\text{eff}} R_s F_N \rho(v) \frac{d_f}{v} dv d\tau, \end{aligned} \quad (\text{B2})$$

where $d\tau$ is the size of time bins for coincidences. The correlated term comes from atoms with velocity $v_\tau = \frac{d \pm d_f}{\tau} \approx \frac{d}{\tau}$. We ignore d_f here since $\frac{d_f}{d}$ is small; these atoms emitted

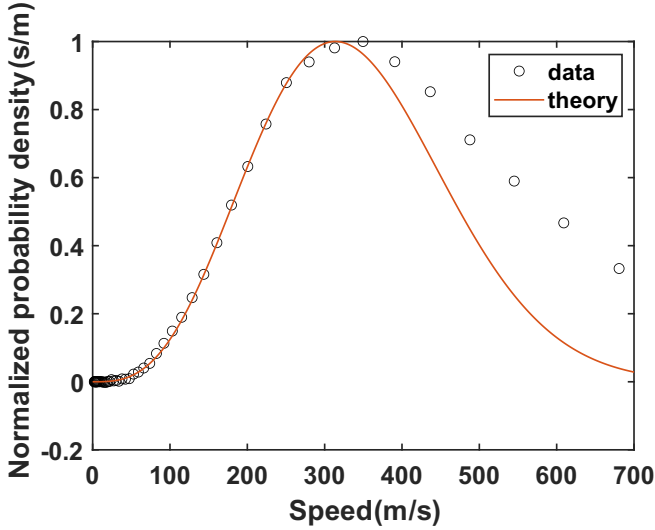


FIG. 7. Plot of the 70 °C thermal atomic beam experimental data after processing versus theory. The distance between the two fibers in the objective plane $d = 55 \mu\text{m}$.

photons in fiber A and in fiber B at τ later:

$$C_{\text{eff}} R_s \frac{d_f}{v_\tau} C_{\text{eff}} R_s \frac{d_f}{v_\tau} F_N \rho(v_\tau) dv_\tau. \quad (\text{B3})$$

Since $v_\tau = \frac{d}{\tau}$, putting $dv_\tau = d\tau \frac{v_\tau^2}{d}$ into (B3), we get

$$(\text{correlated term}) = C_{\text{eff}}^2 R_s^2 \frac{d_f^2}{d} F_N \rho(v_\tau) d\tau. \quad (\text{B4})$$

If we divided the uncorrelated term (B2) on both sides of (B1) and combine the definition of average atom number $\langle N \rangle$ [Eq. (A3)] we get

$$C'(\tau) = 1 + \frac{\frac{d_f}{d} \rho(v_\tau)}{\langle N \rangle \int_v \frac{\rho(v)}{v} dv}. \quad (\text{B5})$$

This formula shows that it needs to be in the single-atom regime ($\langle N \rangle \ll 1$) so that the second correlated term is large enough to be detected.

We can also see that when $\tau \rightarrow \infty$, $C'(\tau) \rightarrow 1$. Since $g_{AB}^{(2)}(\tau)$ is also the coincidence distribution normalized to the infinite time delay, $C'(\tau)$ equals the cross correlation $g_{AB}^{(2)}(\tau)$.

Next, as we mentioned in the main text, that value $g_{AB}^{(2)}(\tau) - g_{AB}^{(2)}(\infty)$, after normalization, is the coincidence probability density from atoms in time domain $n_{AB}(\tau)$, which is proportional to $\rho(v_\tau)$. Given $n_{AB}(\tau) d\tau = n_{AB}(v) dv$ and $\tau = \frac{d}{v}$, we can get the coincidence probability density in velocity space $n_{AB}(v) = n_{AB}(\tau) \frac{d}{v^2}$. Finally, we can get $n_{AB}(v) \propto \rho(v) \frac{1}{v^2}$.

To calibrate our theory with data, we measured the unfiltered thermal atomic beam at 70 °C with our two-fiber detector. The result is shown in Fig. 7. The circles are the experimental data after processing and the red curve is the theoretical curve for the 70 °C atomic beam Maxwell-Boltzmann distribution. The theory fits very well for velocities below 300 m/s, which is the range we focused on. The error becomes

larger when the velocity is higher because $d_f/d \approx 0.45$ and it could have an uncertainty error around 22.5%. Also, because of the imperfect imaging, some atoms can emit photons into both fibers during the transit from fiber A to fiber B , which causes some spurious population at high velocity.

For $\Delta = -20$ and -10 MHz, as mentioned in the main text, the contribution from fast unpumped atoms and vapor is more than that from the selected atoms. Thus we also measured $g_b^{(2)}(\tau)$ with the pump beam and probe beam only to get the contributions from fast unpumped atoms and vapor. Then we subtracted the background contribution when calculating $\rho(v)$ with the selected atoms according to (B5) and assuming $\int_v \frac{\rho(v)}{v} dv$ has roughly the same value.

The Monte Carlo wave-function (MCWF) simulation is also implemented to test our theory. The MCWF simulation was designed to mimic what happened in our experimental system to calculate the $g^{(3)}(\tau_1, \tau_2)$. The atoms are generated according to the Poisson distribution, and the velocities are chosen from the 78 °C atomic beam Maxwell-Boltzmann distribution. The atoms then fly into a laser beam and interact with it. The wave functions are evolved according to the MCWF procedure [33]. When atoms are within the field of view of the fiber, their emitted photons' time tags are registered and stored. Then the same algorithm used to calculate experimental $g^{(3)}(\tau_1, \tau_2)$ is used on the simulation data.

The result is shown in Fig. 8. The color bar is in linear scale and the simulation fits the data quite well. Because of the limited three-photon coincidence rate, Fig. 8 and the $g^{(3)}(\tau_1, \tau_2)$ in our main text all used $100 \times 100 \text{ ns}^2$ time bins to have more averaging effect to overcome the shot noise. The resolution is limited, and the dynamics inside the $100 \times 100 \text{ ns}^2$ is averaged out. Thus, MCWF simulations were done to calculate the $g^{(3)}(\tau_1, \tau_2)$ with no dead time and with $1 \times 1 \text{ ns}^2$ time resolution near zero time delay [Fig. 9(a)]. We can see that similar to $g^{(2)}(0)$, $g^{(3)}(0, 0) = 1$ and when $\tau_1 = 0$, $\tau_2 = 0$, or $\tau_1 = \tau_2$, $g^{(3)}(\tau_1, \tau_2)$ equals 1. Then $g^{(3)}(\tau_1, \tau_2)$ has a huge peak where three consecutive photons from the same atom create coincidences. With 100-ns resolution, this dynamics is averaged into one bunching peak around zero time delay. One can put some graphite in the system to absorb the accumulated vapor and average for a much longer time to reduce the three-photon-coincidence shot noise. Then one can use three detectors to eliminate the dead-time constraint and use a smaller time bin (4 ns) to see the dynamics near zero time delay.

Similar simulations are also done for $g^{(2)}(\tau)$; the result agrees well with our theory in Appendix A (see Fig. 9).

APPENDIX C: CONCATENATED SINGLE-PHOTON STATES FROM TRACKED ATOMS

Here we propose a method to generate photon pairs by the concatenation protocol described in the Introduction. We refer the reader to Fig. 1(c). As described earlier, we first choose two source cells, 1 and 2, and then apply the tracking method to herald the occupation of both cells by atoms at a known instant of time. This can be accomplished by detecting a pair of photons from two detectors placed upstream of the cells

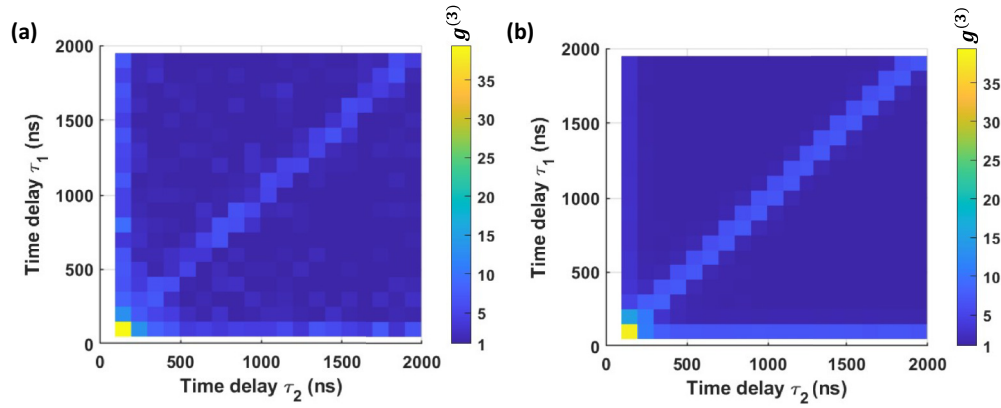


FIG. 8. (a) Experimental $g^{(3)}(\tau_1, \tau_2)$ value for the 78 °C unfiltered thermal atomic beam. This figure is the same as Fig. 5(a) in linear scale. (b) Simulated $g^{(3)}(\tau_1, \tau_2)$. The time bin size is $100 \times 100 \text{ ns}^2$.

and then waiting a fixed amount of time before the atoms enter the cells. Since the atoms move slowly, this should be feasible with microsecond update times, and the single-photon camera itself could potentially be used for both heralding and measurement. Once the atoms have entered the cells, a short excitation pulse of light of duration τ_p will cause each of these atoms to spontaneously generate a single photon. If $|n_i\rangle$ is a Fock state of n_i photons emitted from cell i , then the state $|1_1, 1_2\rangle$ will be a concatenation of single-photon states, one each from cells 1 and 2. This state has a nontrivial spatial distribution since each origination cell corresponds to a different spatial mode for the propagating photon. In this way it is similar to spontaneous down-conversion sources that are frequently used in quantum imaging and information processing [34]. We consider applications of our light source to illuminating a target [see Fig. 1(c)], where we detect correlations between the two photons. Apart from being a general purpose quantum light source, it may prove especially well suited to targets consisting of trapped ultracold Rb atoms.

To establish the feasibility of our proposal as a proof of concept, we show below that the probability of pair

generation in the state $|1_1, 1_2\rangle$ exceeds that of spurious two-photon generation from one cell, $|2_1, 0_2\rangle$ and $|0_1, 2_2\rangle$, as well as unpaired single-photon states $|1_1, 0_2\rangle$ and $|0_1, 1_2\rangle$ that represent background Poisson noise. Thus the density matrix of the pair will have a high degree of purity. This can be quantified and benchmarked using the usual methodologies, for instance, Hong-Ou-Mandel interference performed by recombining the output of both cells using a beam splitter and two SPCMs [31]. For the purpose of this paper, we simply wish to demonstrate that such a quantum light source is feasible. Hence, we establish bounds on the purity by calculating the probabilities classically.

We define $Q_i(n_i)$ to be the probability to collect n_i photons from cell i within an observation time window T_w after the excitation pulse τ_p . For a perfect single-photon source $Q_i(1) = 1$. We assume that τ_p is a Rabi π pulse, with $\tau_p \ll 1/\Gamma$ and $T_w \gg 1/\Gamma$. The former condition ensures that no more than one photon is emitted by an atom, while the latter condition ensures that zero-photon emission is not a possibility. Very similar conditions are employed for single-photon sources such as quantum dots [35], although here our atom sources have a built-in indistinguishability that is not present

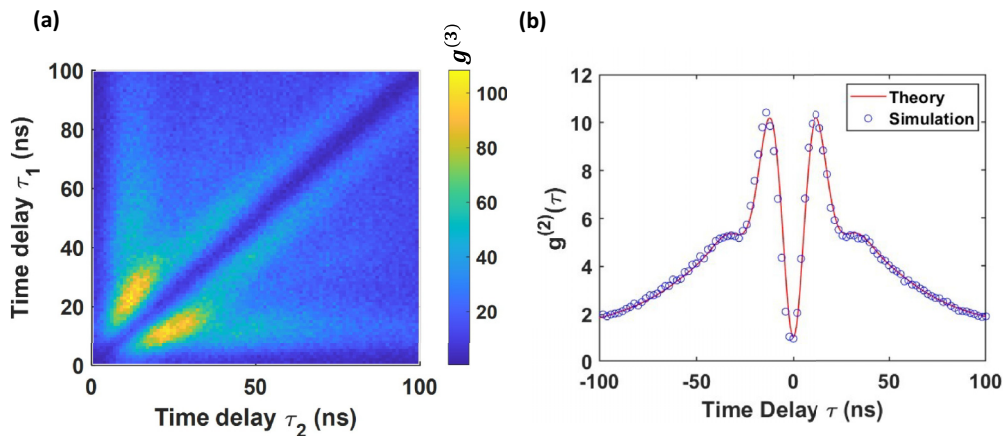


FIG. 9. (a) Simulated $g^{(3)}(\tau)$ with $1 \times 1 \text{ ns}^2$ time bins to see the dynamics near zero time delay. (b) Simulated $g^{(2)}(\tau)$ with the same parameter we used to fit our experimental data, plotted together with our theoretical curve. Here $\langle N \rangle = 0.138$, $L = 25 \text{ }\mu\text{m}$, and Ω is a Gaussian distribution with $\mu = 6\Gamma$ and $\sigma = 1.5\Gamma$.

in any solid-state system. Thus we may assume that each atom is a perfect single-photon emitter, although we still maintain a finite photon collection efficiency $0 < \eta < 1$ that is assumed to be the same for each cell. The probability to receive k photons from a cell containing m atoms is given by the binomial formula $C_{mk}\eta^k(1-\eta)^{m-k}$, where $C_{mk} = m!/k!(m-k)!$. If $P_i(m)$ is the probability that cell i is occupied by m atoms, then the probabilities of collecting zero, one, and two photons from cell i are then easily expressed as

$$\begin{aligned} Q_i(0) &= \sum_{m=0}^{\infty} P_i(m)C_{m0}(1-\eta)^m, \\ Q_i(1) &= \sum_{m=1}^{\infty} P_i(m)C_{m1}\eta(1-\eta)^{m-1}, \\ Q_i(2) &= \sum_{m=2}^{\infty} P_i(m)C_{m2}\eta^2(1-\eta)^{m-2}. \end{aligned}$$

It is straightforward to simplify the above as

$$\begin{aligned} Q_i(0) &= \sum_{m=0}^{\infty} P_i(m)(1-\eta)^m, \\ Q_i(1) &= -\frac{\partial}{\partial \eta} Q_i(0), \\ Q_i(2) &= \frac{\eta^2}{2} \frac{\partial^2}{\partial \eta^2} Q_i(0). \end{aligned} \quad (\text{C1})$$

We now define the signal-to-noise ratios

$$\begin{aligned} \left(\frac{S}{N}\right)_{22} &= \frac{Q_1(1)Q_2(1)}{Q_1(0)Q_2(2) + Q_1(2)Q_2(0)}, \\ \left(\frac{S}{N}\right)_{21} &= \frac{Q_1(1)Q_2(1)}{Q_1(0)Q_2(1) + Q_1(1)Q_2(0)}. \end{aligned} \quad (\text{C2})$$

A large value of $(S/N)_{22}$ signifies a high purity for the pair state $|1_1, 1_2\rangle$ and low probability of occupying spurious two-photon states. Moreover, a large value of $(S/N)_{21}$ is needed to suppress unpaired single-photon states. For the distributions concerned here, all quantities can be analytically evaluated, but to illustrate the physics we will present many of the results only to leading order in the mean atom occupation probability $p \ll 1$.

Without heralding, we have a Poisson distribution of atom occupancy probabilities $P_i(m) = e^{-p}p^m/m!$ with mean occupancy p . Putting this expression into Eqs. (C1) and (C2), we

obtain

$$\begin{aligned} \left(\frac{S}{N}\right)_{22} &= 1, \\ \left(\frac{S}{N}\right)_{21} &= \frac{p\eta}{2}. \end{aligned} \quad (\text{C3})$$

Without heralding, the two photons are equally likely to come from two atoms in one cell as they are to come from one atom in each cell; hence $(S/N)_{22} = 1$. Moreover, for $p \ll 1$ the probability of singles far exceeds the pair rate; hence $(S/N)_{21} \ll 1$. This unheralded regime makes for a good single-photon source, but not a great source of pairs.

With heralding, the situation changes considerably for pair production. No longer is it possible to have an unoccupied cell, so $P_i(0) = 0$. This considerably reduces the likelihood of receiving no photons at all and therefore also the probability of generating the spurious two-photon states $|2_1, 0_2\rangle$ and $|0_1, 2_2\rangle$. We conservatively assume that the heralding yields no new information on the probability distribution for $P_i(m > 1)$,¹ in which case the new distribution is simply a renormalization of the original Poisson distribution with the $m = 0$ component removed, i.e.,

$$P_i(0) = 0, \quad P_i(m > 0) = \left(\frac{1}{e^p - 1}\right) \frac{p^m}{m!}, \quad (\text{C4})$$

with $\sum_{m=1}^{\infty} P_i(m) = 1$. Putting this expression into Eqs. (C1) and (C2) yields

$$\begin{aligned} \left(\frac{S}{N}\right)_{22} &= \frac{1}{p(1-\eta)} + \frac{1}{2} + O(p), \\ \left(\frac{S}{N}\right)_{21} &= \frac{\eta}{2(1-\eta)} + O(p), \end{aligned} \quad (\text{C5})$$

and if $p \ll 1$, $(\frac{S}{N})_{22} > 1/p \gg 1$, so the pair state $|1_1, 1_2\rangle$ is much more likely than either of the spurious two-photon states $|2_1, 0_2\rangle$ and $|0_1, 2_2\rangle$. The intuitive explanation for the suppression is that both sites contain at least one atom. Moreover, for high collection efficiency $\eta \rightarrow 1$, $(\frac{S}{N})_{21} \gg 1$, so the probability of receiving unpaired photons diminishes. We note that finite detection efficiency is not unique to our system, as it affects all types of pair sources, including spontaneous down-conversion sources. It should not unduly affect the utility of our source. This shows that the tracking features will allow one to realize novel, spatially resolved photon-pair states with utility in quantum information applications.

¹In fact, the probability that $m > 1$ is reduced by heralding, which only improves the outcome. Using Poisson statistics, we can infer that the probability that one heralding photon was received from one atom is approximately equal to $p\eta$, while the probability it was received from two atoms is approximately equal to $p^2\eta(1-\eta)$, i.e., smaller by the factor $p(1-\eta) < 1$.

[1] C. Shu, P. Chen, T. K. A. Chow, L. Zhu, Y. Xiao, M.T. Loy, and S. Du, *Nat. Commun.* **7**, 12783 (2016).

[2] T.-M. Zhao, Y. S. Ihn, and Y.-H. Kim, *Phys. Rev. Lett.* **122**, 123607 (2019).

- [3] F. E. Becerra, R. T. Willis, S. L. Rolston, and L. A. Orozco, *Phys. Rev. A* **78**, 013834 (2008).
- [4] D. Main, T. M. Hird, S. Gao, E. Oguz, D. J. Saunders, I. A. Walmsley, and P. M. Ledingham, *Phys. Rev. A* **103**, 043105 (2021).
- [5] J. T. Wilson, S. Saskin, Y. Meng, S. Ma, R. Dilip, A. P. Burgers, and J. D. Thompson, *Phys. Rev. Lett.* **128**, 033201 (2022).
- [6] A. M. Kaufman and K.-K. Ni, *Nat. Phys.* **17**, 1324 (2021).
- [7] C. D. Bruzewicz, J. Chiaverini, R. McConnell, and J. M. Sage, *Appl. Phys. Rev.* **6**, 021314 (2019).
- [8] K. Singer, U. Poschinger, M. Murphy, P. Ivanov, F. Ziesel, T. Calarco, and F. Schmidt-Kaler, *Rev. Mod. Phys.* **82**, 2609 (2010).
- [9] M. Brune, E. Hagley, J. Dreyer, X. Maitre, A. Maali, C. Wunderlich, J. M. Raimond, and S. Haroche, *Phys. Rev. Lett.* **77**, 4887 (1996).
- [10] M. Brune, F. Schmidt-Kaler, A. Maali, J. Dreyer, E. Hagley, J. M. Raimond, and S. Haroche, *Phys. Rev. Lett.* **76**, 1800 (1996).
- [11] P. Maioli, T. Meunier, S. Gleyzes, A. Auffeves, G. Nogues, M. Brune, J. M. Raimond, and S. Haroche, *Phys. Rev. Lett.* **94**, 113601 (2005).
- [12] D. Pizzey, J. D. Briscoe, F. D. Logue, F. S. P. Ojeda, S. A. Wrathmall, and I. G. Hughes, *New J. Phys.* **24**, 125001 (2022).
- [13] O. Wolley, T. Gregory, S. Beer, T. Higuchi, and M. Padgett, *Sci. Rep.* **12**, 8286 (2022).
- [14] D. Shin, F. Xu, D. Venkatraman, R. Lussana, F. Villa, F. Zappa, V. K. Goyal, F. N. C. Wong, and J. H. Shapiro, *Nat. Commun.* **7**, 12046 (2016).
- [15] C. Couteau, *Contemp. Phys.* **59**, 291 (2018).
- [16] J. Sabines-Chesterking, R. Whittaker, S. K. Joshi, P. M. Birchall, P.-A. Moreau, A. McMillan, H. V. Cable, J. L. O'Brien, J. G. Rarity, and J. C. F. Matthews, *Phys. Rev. Appl.* **8**, 014016 (2017).
- [17] C. Li, X. Chai, B. Wei, J. Yang, A. Daruwalla, F. Ayazi, and C. Raman, *Nat. Commun.* **10**, 1831 (2019).
- [18] H. J. Kimble, M. Dagenais, and L. Mandel, *Phys. Rev. Lett.* **39**, 691 (1977).
- [19] R. Loudon, *The Quantum Theory of Light* (Oxford University Press, Oxford, 2000).
- [20] H. J. Kimble, M. Dagenais, and L. Mandel, *Phys. Rev. A* **18**, 201 (1978).
- [21] F. Diedrich and H. Walther, *Phys. Rev. Lett.* **58**, 203 (1987).
- [22] S. Gerber, D. Rotter, L. Slodička, J. Eschner, H. J. Carmichael, and R. Blatt, *Phys. Rev. Lett.* **102**, 183601 (2009).
- [23] M. K. Tey, Z. Chen, S. A. Aljunid, B. Chng, F. Huber, G. Maslennikov, and C. Kurtsiefer, *Nat. Phys.* **4**, 924 (2008).
- [24] S. Du, J. Wen, M. H. Rubin, and G. Y. Yin, *Phys. Rev. Lett.* **98**, 053601 (2007).
- [25] S. Ribeiro, T. F. Cutler, C. S. Adams, and S. A. Gardiner, *Phys. Rev. A* **104**, 013719 (2021).
- [26] S.-Y. Baek and Y.-H. Kim, *Phys. Rev. A* **77**, 043807 (2008).
- [27] M. Khoshnegar, T. Huber, A. Predojević, D. Dalacu, M. Prilmüller, J. Lapointe, X. Wu, P. Tamarat, B. Lounis, P. Poole *et al.*, *Nat. Commun.* **8**, 15716 (2017).
- [28] S. Krapick, B. Brecht, H. Herrmann, V. Quiring, and C. Silberhorn, *Opt. Express* **24**, 2836 (2016).
- [29] H. Hübel, D. R. Hamel, A. Fedrizzi, S. Ramelow, K. J. Resch, and T. Jennewein, *Nature (London)* **466**, 601 (2010).
- [30] A. Kuhn and D. Ljunggren, *Contemp. Phys.* **51**, 289 (2010).
- [31] C.-K. Hong, Z.-Y. Ou, and L. Mandel, *Phys. Rev. Lett.* **59**, 2044 (1987).
- [32] D. A. Steck, *Quantum and atom optics* (2007), available at <https://atomoptics.uoregon.edu/~dsteck/teaching/quantum-optics/>.
- [33] K. Mølmer, Y. Castin, and J. Dalibard, *J. Opt. Soc. Am. B* **10**, 524 (1993).
- [34] P.-A. Moreau, E. Toninelli, T. Gregory, and M. J. Padgett, *Nat. Rev. Phys.* **1**, 367 (2019).
- [35] C.-Y. Lu and J.-W. Pan, *Nat. Nanotechnol.* **16**, 1294 (2021).